

# Multi-band luminosity correlation analysis for Fermi blazars

Le-Jian OU,<sup>1,2,3</sup> Jun-Hui FAN,<sup>1,2,3,\*†</sup> and Yu-hai YUAN<sup>1,2,3</sup>

<sup>1</sup>Center for Astrophysics, Guangzhou University, Guangzhou, 510006, China

<sup>2</sup>Greater Bay Brand Center of the National Astronomical Data Center, Guangzhou 510006, China

<sup>3</sup>Astronomy Science and Technology Research Laboratory of Department of Education of Guangdong Province, Guangzhou 510006, China

\*E-mail: [fjh@gzhu.edu.cn](mailto:fjh@gzhu.edu.cn)

†230 Wai Huan Xi Road, Guangzhou Higher Education Mega Center, Guangzhou 510006, China

## Abstract

Multi-band and  $\gamma$ -ray radiation are important properties of blazars. In this paper, the luminosity correlations between the  $\gamma$ -ray and lower-energy (radio, optical, and X-ray) bands for both the observed and intrinsic data are investigated using the multiple linear regression analysis for a sample of 642 blazars (227 flat spectrum radio quasars and 415 BL Lacertae objects). In addition, we employ a partial correlation analysis to exclude the redshift effect in the mutual correlation analysis. We also investigate the intrinsic luminosity correlations using the second-order partial correlation analysis to exclude the effects of redshift and Doppler factor, which has allowed us to obtain the intrinsic correlation without the influence of relativistic beaming effect or redshift. We find that both the observed and intrinsic  $\gamma$ -ray emissions are correlated with the radio, optical, and the X-ray bands, with the radio and optical bands being important for the  $\gamma$ -ray emissions, indicating that the  $\gamma$ -ray emissions originate from the lepton model, including self-synchrotron Compton and external Compton processes.

**Keywords:** BL Lacertae objects: general — galaxies: active — galaxies: jets — quasars: general

## 1 Introduction

Blazars, which are the most extreme special subclass of active galactic nuclei (AGNs), have a variety of extreme observational properties, such as high luminosity, high and variable polarization, core-dominated non-thermal continuums, superluminal motions, and strong  $\gamma$ -ray emissions, etc. (Antonucci & Ulvestad 1985; Webb 1992; Vermeulen & Cohen 1994; Urry & Padovani 1995; Abdo et al. 2010; Ackermann et al. 2015; Fan et al. 2016; Ajello et al. 2022; Xiao et al. 2022b; Bachev et al. 2023). Fan et al. (2013) proposed the  $\gamma$ -ray emissions as an observational property of blazars. In the unification model of AGNs, there is a supermassive black hole (SMBH) surrounded by an accretion disk. Blazars emit emissions through the entire electromagnetic spectrum, from the radio bands to the  $\gamma$ -rays (Fossati et al. 1998). The extreme properties are due to a relativistic jet pointing along our line of sight, resulting in the blazars being the most luminous AGNs.

Based on the equivalent width ( $EW$ ) of emission lines, blazars are classified into two groups: BL Lacertae objects and flat spectrum radio quasars, hereafter BLLs and FSRQs, respectively (Angel & Stockman 1980). BLLs are characterized by weak or absent emission lines ( $EW < 5 \text{ \AA}$ ) while FSRQs have prominent emission lines ( $EW > 5 \text{ \AA}$ ) (Padovani & Urry 1991). Ghisellini et al. (2011) proposed that the sources with  $\log L_{\text{BLR}}/L_{\text{Edd}} < 5 \times 10^{-4}$  are BLLs and those with  $\log L_{\text{BLR}}/L_{\text{Edd}} > 5 \times 10^{-4}$  are FSRQs. In contrast, Xiao et al. (2022a) used a machine-learning method to separate BLLs and FSRQs in the plot of  $\log L_{\text{BLR}}/L_{\text{Edd}}$  against  $\log L_{\gamma}/L_{\text{Edd}}$  with a dividing line of  $\log(L_{\text{BLR}}/L_{\text{Edd}}) = 0.25 \log(L_{\gamma}/L_{\text{Edd}}) - 2.23$ . Here,  $L_{\text{BLR}}$  is the luminosity of the broad-line region,  $L_{\gamma}$  is the  $\gamma$ -ray luminosity, and  $L_{\text{Edd}}$  is the Eddington lumi-

nosity, defined as the maximum luminosity at which radiation pressure balances the gravitational attraction.

The spectral energy distributions (SEDs) of blazars show a double peak structure: the low-energy peak is from the synchrotron emission while the high-energy peak is from the inverse Compton (IC) emission (Padovani & Giommi 1995). The low-energy peak is located at the far-infrared to X-ray bands, while the high-energy peak is at the MeV to TeV bands. Based on the synchrotron peak frequency in SEDs, Abdo et al. (2010) classified blazars into low synchrotron peak sources (LSPs), intermediate synchrotron peak sources (ISPs), and high synchrotron peak sources (HSPs), with the logarithmic synchrotron peak frequency boundaries [ $\log(\nu_p/\text{Hz})$ ] of 14 and 15. More accurately, using a machine-learning Bayesian Gaussian mixture model to fit the distribution of the logarithm of the synchrotron peak frequency in the source frame, Fan et al. (2016) and Yang et al. (2022a) classified the Fermi/LAT 3FGL 1392 blazars and 4FGL 2709 blazars into LSPs, ISPs, and HSPs, with the boundaries of  $\log(\nu_p/\text{Hz}) = 14.0$  and  $15.3$  in 3FGL, or  $\log(\nu_p/\text{Hz}) = 13.7$  and  $14.9$  in 4FGL, respectively. Therefore, we can say boundary frequencies are about 14 and 15.

The Fermi/LAT has detected a large number of  $\gamma$ -ray sources since it was launched in 2008, and the vast majority of the detected AGN sources are blazars (Abdo et al. 2010; Ackermann et al. 2015; Ajello et al. 2022). In blazars, the dominant radiation mechanisms in the low-energy band are the synchrotron process, while the IC process predominantly governs the high-energy band, particularly in the  $\gamma$ -ray regime. The mechanisms of the  $\gamma$ -ray emissions of blazars have been studied by many researchers, but there is no consensus. The

Received: 2025 April 8; Accepted: 2025 August 26

© The Author(s) 2025. Published by Oxford University Press on behalf of the Astronomical Society of Japan. All rights reserved. For commercial re-use, please contact [reprints@oup.com](mailto:reprints@oup.com) for reprints and translation rights for reprints. All other permissions can be obtained through our RightsLink service via the Permissions link on the article page on our site—for further information please contact [journals.permissions@oup.com](mailto:journals.permissions@oup.com)

lepton and baryon models are proposed to explain the origination of the  $\gamma$ -rays in blazars. In the lepton model, the  $\gamma$ -rays originate from the relativistic jets through the IC process, including the synchrotron self-Compton (SSC) model and the external Compton mechanism (EC) model, where the photons come from the synchrotron emissions inside the jet in the former case and the latter comes from outside the jet (Maraschi et al. 1992; Sikora et al. 1994). In the baryon models, the  $\gamma$ -rays are from the collision of protons with protons or photons with photons (Dermer & Schlickeiser 1993; Beall & Bednarek 1999). Under the one-zone SSC model, the seed photons for the  $\gamma$ -ray emission originate from synchrotron radiation and are upscattered via IC processes in the same emission region (Konigl 1981; Marscher & Gear 1985), leading to a positive correlation between the  $\gamma$ -ray and lower-energy bands. In a mixed SSC + EC model, where a fraction of the  $\gamma$ -ray seed photons originate from external radiation fields (Dermer & Schlickeiser 1993; Bloom & Marscher 1996), a positive correlation is expected. In contrast, under hadronic models, the low-energy emission is mainly produced by synchrotron radiation from electrons, while the high-energy emission is dominated by proton synchrotron radiation,  $\pi^0$  decay photons, and subsequent synchrotron or IC emission from secondary particles (Mannheim & Biermann 1992; Aharonian 2000). As a result, no clear correlation is generally expected between the  $\gamma$ -ray and lower-energy bands. The different radiation models imply different correlations between the  $\gamma$ -rays and the lower-energy bands (radio, optical, and X-ray), so it is possible to use these correlations to study the  $\gamma$ -ray emission mechanism (Dondi & Ghisellini 1995; Fossati et al. 1998; Hovatta et al. 2014; Fan et al. 2016; Fallah Ramazani et al. 2017; Zhang et al. 2018).

Fan (1996) used multiple linear regression analysis to investigate the correlations between the  $\gamma$ -rays and the low-energy bands using a form of  $Y = a + bX_1 + cX_2 + dX_3$  for a sample of 28 blazars. They found that the radio band holds the most importance for the  $\gamma$ -ray emissions. This analysis discloses the importance between independent variables  $X_i$  (i.e.,  $L_R$ ,  $L_O$ ,  $L_X$ ) and the dependent variable  $Y$  (i.e.,  $L_\gamma$ ). Here, the  $L_R$ ,  $L_O$ ,  $L_X$ , and  $L_\gamma$  correspond to the luminosities in the radio, optical, X-ray, and the  $\gamma$ -ray bands, respectively. The correlation coefficient  $r$  shows the fitting of regression, indicating a positive correlation, an anticonnection, and no correlations with  $r > 0$ ,  $r < 0$ , and  $r \sim 0$ , respectively. The absolute value of  $r$  ( $|r| \leq 1$ ) represents the degree of fitting, where greater  $|r|$  shows better fitting. Correlation significance is expressed by a chance probability parameter  $p$ . Note that  $p < 0.05$  indicates a significant correlation, while  $p > 0.05$  means that the predictor does not have a significant effect on the dependent variable. The parameter  $a$  is a constant;  $b$ ,  $c$ , and  $d$  are the regression coefficients for  $X_1$ ,  $X_2$ , and  $X_3$ . The parameter  $T$ -values ( $T_i$ ) are commonly used to assess the contribution of each independent variable in a regression model (Cohen 1988). The  $T$ -value is calculated using the formula  $T = \hat{\epsilon}/\epsilon_{\text{error}}$ , where  $\hat{\epsilon}$  is the estimated regression coefficient, and  $\epsilon_{\text{error}}$  is the standard error of the regression coefficient estimate. A larger  $T$ -value indicates a more significant influence of the predictor variable on the dependent variable. Typically, a  $T$ -value greater than 2.0 or 1.0 suggests that the predictor variable is of substantial or moderate importance for the dependent variable  $Y$ . By comparing the importance of  $X_i$  and  $X_j$ , it can be concluded that  $X_i$  is more important than  $X_j$  for  $Y$  if  $T_i > T_j > 1.0$ . However, Fan (1996) only investigated a sample of 28 sources. Later,

Zhang et al. (2018) investigated a sample of 442 sources using a similar correlation analysis method. They found that  $\gamma$ -ray emissions are correlated with all the lower-energy bands, with the radio band holding the most importance, followed by the optical band.

Due to the beaming effect, blazars show remarkable observational characteristics (Urry & Padovani 1995; Dondi & Ghisellini 1995; Fan et al. 2017; Yang et al. 2022b). The observed luminosity will be more luminous than the intrinsic luminosity because of the relativistic Doppler enhancement. From the relativistic beaming model, the intrinsic (or de-beamed) luminosity  $L_v^{\text{inc}}$  for a continuous jet or  $L_v^{\text{ins}}$  for a spherical jet (Marscher & Gear 1985; Blandford & Königl 1979) can be calculated by  $L_v^{\text{inc}} = L_v^{\text{ob}}/\delta^{3+\alpha_v}$ , or  $L_v^{\text{ins}} = L_v^{\text{ob}}/\delta^{4+\alpha_v}$  for a spherical jet (Fan et al. 2017). Here,  $L_v^{\text{ob}}$  is the observed luminosity,  $\alpha$  is a spectral index at the corresponding band ( $f \propto v^{-\alpha}$ ),  $\delta$  is the Doppler factor expressed as  $\delta = 1/[\Gamma(1 - \beta \cos \theta)]$ ,  $\theta$  is the angle between the jet and the line of sight,  $\beta$  is the jet velocity in the units of the speed of light, and  $\Gamma$  is the Lorentz factor. The corresponding intrinsic frequency for a continuous jet ( $v^{\text{inc}}$ ) and a spherical jet ( $v^{\text{ins}}$ ) can be calculated in  $v^{\text{inc}} = v^{\text{ins}} = v^{\text{ob}}/[\delta/(1+z)]$ , in which  $v^{\text{ob}}$  is the observed frequency and  $z$  is a redshift.

With the latest 4LAC-DR3<sup>1</sup> Fermi AGN catalog, there are 755 FSRQs and 1379 BLLs (Ajello et al. 2022), which provides us with an opportunity to study the correlation between the  $\gamma$ -ray and the lower-energy bands based on an even larger sample and the de-beamed data. The paper structure is as follows: in section 2, we give details of the sample and discuss the results; in section 3, we discuss the observed and intrinsic luminosity correlations; we conclude in section 4.

## 2 Sample and results

We extracted a sample of 642 Fermi blazars (227 FSRQs and 415 BLLs) from the catalog of 2709 blazars compiled by Yang et al. (2022a), based on available radio, optical, X-ray, and  $\gamma$ -ray luminosities ( $L_R$ ,  $L_O$ ,  $L_X$ , and  $L_\gamma$ ), as well as the known redshift ( $z$ ). The luminosity data in all four bands were directly adopted from Yang et al. (2022a), where Galactic extinction for the optical band and Galactic absorption corrections for the soft X-ray band were applied. The luminosity data have also been subjected to K-correction but have not considered the non-jet emission components. The representative frequencies of the four bands are at 1.4 GHz (radio),  $2.43 \times 10^{14}$  Hz (optical), 1 keV (X-ray), and 1 GeV ( $\gamma$ -ray). For the present sample, we gathered Doppler factors for 353 blazars from Chen et al. (2024). In the present work, the Doppler factor exhibits an average value of  $\bar{\delta} = 12.47$  (range 0.84–84.88), with the first quartile  $Q_1 = 4.81$ , median  $Q_2 = 8.48$ , and the third quartile  $Q_3 = 15.67$ ; compared with  $\bar{\delta} = 12.99$  (range 0.45–88.52),  $Q_1 = 5.47$ ,  $Q_2 = 9.11$ , and  $Q_3 = 15.74$  in Chen et al. (2024). The Doppler factor distribution in the present work is statistically consistent with those in Chen et al. (2024), with Kolmogorov–Smirnov (KS) test statistics  $D = 0.052$  and significance  $P = 0.469$ .

Adapting the classification by Yang et al. (2022a)—LSPs, ISPs, and HSPs correspond to  $\log v_s^p(\text{Hz}) < 13.7$ ,  $13.7 < \log v_s^p(\text{Hz}) < 14.9$ , and  $\log v_s^p(\text{Hz}) > 14.9$ , respectively—we have 38 LSP-BLLs (LBLs), 88 ISP-BLLs (IBLs), 289 HSP-BLLs (HBLs), 185 LSP-FSRQs (LFs), 40 ISP-FSRQs (IFs),

<sup>1</sup> <https://fermi.gsfc.nasa.gov/ssc/data/access/lat/4LACDR3/>.

**Table 1.** Average values and standard deviations in different subclasses.\*

Class (1)	Num (2)	$\log L_R$ (3)	$\log L_O$ (4)	$\log L_X$ (5)	$\log L_\gamma$ (6)	$\bar{z}$ (7)	$\log v_p$ (8)	$\log L_p$ (9)
ALL	642	$42.07 \pm 1.32$	$45.13 \pm 0.84$	$44.65 \pm 1.00$	$44.92 \pm 1.31$	$0.62 \pm 0.54$	$14.68 \pm 1.31$	$45.32 \pm 0.94$
FSRQ	227	$43.33 \pm 0.79$	$45.66 \pm 0.66$	$44.98 \pm 0.78$	$45.94 \pm 1.01$	$0.97 \pm 0.54$	$13.26 \pm 0.51$	$45.92 \pm 0.72$
BLL	415	$41.41 \pm 1.00$	$44.86 \pm 0.77$	$44.51 \pm 1.01$	$44.40 \pm 1.07$	$0.44 \pm 0.43$	$15.46 \pm 1.13$	$45.02 \pm 0.86$
LBL	38	$42.89 \pm 0.91$	$45.24 \pm 0.80$	$44.66 \pm 0.94$	$45.59 \pm 0.98$	$0.70 \pm 0.42$	$13.25 \pm 0.25$	$45.64 \pm 0.87$
HBL	289	$41.06 \pm 0.79$	$44.75 \pm 0.74$	$44.62 \pm 0.99$	$44.14 \pm 0.98$	$0.40 \pm 0.40$	$16.07 \pm 0.67$	$45.93 \pm 0.83$
LF	185	$43.42 \pm 0.74$	$45.71 \pm 0.64$	$45.08 \pm 0.74$	$46.03 \pm 0.99$	$1.01 \pm 0.54$	$13.08 \pm 0.32$	$46.00 \pm 0.68$
HSP	291	$41.06 \pm 0.80$	$44.74 \pm 0.74$	$44.60 \pm 0.99$	$44.13 \pm 0.99$	$0.39 \pm 0.40$	$16.06 \pm 0.66$	$44.92 \pm 0.83$
ISP	135	$42.20 \pm 1.03$	$45.15 \pm 0.80$	$44.19 \pm 1.02$	$44.94 \pm 1.12$	$0.56 \pm 0.52$	$14.30 \pm 0.36$	$45.21 \pm 0.90$
LSP	223	$43.30 \pm 0.85$	$45.61 \pm 0.73$	$44.98 \pm 0.86$	$45.93 \pm 1.06$	$0.95 \pm 0.54$	$13.11 \pm 0.31$	$45.92 \pm 0.76$

\*Columns: (1) classification; (2) sample size; (3)–(9) average values for the logarithmic radio luminosity [ $\log(L_R/\text{erg s}^{-1})$ ], logarithmic optical luminosity [ $\log(L_O/\text{erg s}^{-1})$ ], logarithmic X-ray luminosity [ $\log(L_X/\text{erg s}^{-1})$ ], logarithmic  $\gamma$ -ray luminosity [ $\log(L_\gamma/\text{erg s}^{-1})$ ], redshift ( $z$ ), logarithmic synchrotron peak frequency [ $\log(v_p/\text{Hz})$ ], logarithmic synchrotron peak luminosity [ $\log(L_p/\text{erg s}^{-1})$ ], respectively.

**Table 2.** Maximum and minimum values in different subclasses.\*

Class (1)	Num (2)	$\log L_R$ (min) (3)	$\log L_R$ (max) (4)	$\log L_O$ (min) (5)	$\log L_O$ (max) (6)	$\log L_X$ (min) (7)	$\log L_X$ (max) (8)	$\log L_\gamma$ (min) (9)	$\log L_\gamma$ (max) (10)	$z$ (min) (11)	$z$ (max) (12)	$\log v_p$ (min) (13)	$\log v_p$ (max) (14)	$\log L_p$ (min) (15)	$\log L_p$ (max) (16)
ALL	642	38.50	44.76	42.44	47.38	39.97	47.72	41.04	48.10	0.01	4.00	12.11	17.92	42.37	47.74
FSRQ	227	40.89	44.76	43.86	47.38	42.01	46.95	43.03	48.10	0.01	3.10	12.11	15.79	44.06	47.74
BLL	415	38.81	44.09	42.44	47.29	41.72	47.72	42.15	47.42	0.02	4.00	12.86	17.92	42.58	47.61
LBL	38	40.54	44.09	42.91	46.80	42.49	46.26	42.89	47.42	0.05	1.51	12.86	13.66	43.23	47.06
HBL	289	38.81	43.40	42.44	46.91	41.73	47.72	42.18	46.84	0.02	2.15	14.90	17.92	42.58	47.41
LF	185	40.89	44.76	43.86	47.38	42.01	46.95	43.03	48.10	0.01	3.10	12.11	13.68	44.06	47.28
HSP	291	38.81	43.40	42.44	46.91	41.73	47.72	41.92	46.84	0.02	2.15	14.90	17.92	42.58	47.41
ISP	135	38.50	44.62	42.63	47.29	39.97	46.91	41.04	47.36	0.01	4.00	13.71	14.90	42.37	47.74
LSP	223	39.55	44.76	42.85	47.38	42.55	46.95	42.12	48.10	0.02	3.10	12.11	13.68	43.21	47.28

\*Columns: (1) classification; (2) sample size; (3)–(16) minimum and maximum values for the logarithmic radio luminosity [ $\log(L_R/\text{erg s}^{-1})$ ], logarithmic optical luminosity [ $\log(L_O/\text{erg s}^{-1})$ ], logarithmic X-ray luminosity [ $\log(L_X/\text{erg s}^{-1})$ ], logarithmic  $\gamma$ -ray luminosity [ $\log(L_\gamma/\text{erg s}^{-1})$ ], redshift  $z$ , logarithmic synchrotron peak frequency [ $\log(v_p/\text{Hz})$ ], logarithmic synchrotron peak luminosity [ $\log(L_p/\text{erg s}^{-1})$ ], respectively.

and 2 HSP–FSRQs (HFs)—or 291 HSPs, 128 ISPs, and 223 LSPs. We use the relativity continuous jet model and spherical jet model (Fan et al. 2017) to calculate the de-beamed luminosity for the subsample of 353 blazars with Doppler factors. For BLLs, we adopted  $\alpha_R = 0$  and  $\alpha_O = 1.0$  for radio and optical spectral indices, respectively, while for FSRQs, we used  $\alpha_R = 0$  and  $\alpha_O = 0.5$  for radio and optical spectral indices, respectively. In cases where the X-ray spectral index was unavailable, an average value was assumed, with  $\bar{\alpha}_X = 0.78$  for BLLs and  $\bar{\alpha}_X = 1.30$  for FSRQs, as in Fan et al. (2017) and Yang et al. (2022b). The  $\gamma$ -ray spectral indices ( $\alpha_\gamma = \alpha_{\text{ph}} - 1$ , where  $\alpha_{\text{ph}}$  is a photon spectral index) are adopted in the latest 4LAC-DR3 Fermi AGN catalog (Ajello et al. 2022).

For the whole sample, the logarithmic radio luminosity [ $\log(L_R/\text{erg s}^{-1})$ ] ranges from 38.50 to 44.76, with an average value of  $42.07 \pm 1.32$ . For the subclasses, the average, maximum, and minimum values for different bands are presented in tables 1 and 2.

When the multiple linear regression analysis is performed for the whole sample, we have

$$\log L_\gamma = (0.53 \pm 0.03) \log L_R + (0.56 \pm 0.05) \log L_O + (0.14 \pm 0.03) \log L_X - (8.79 \pm 1.10),$$

with a correlation coefficient  $r = 0.93$  and a chance probability  $p < 0.001$ . To investigate which lower-energy band is more important for the  $\gamma$ -ray emission, we calculated the  $T$  values:

$T_R = 20.28$ ,  $T_O = 11.24$ , and  $T_X = 4.99$  for radio, optical, and the X-ray bands, respectively. The method is performed for the FSRQ, BLL, LBL, HBL, LF, LSP, and HSP subclasses (here, we did not consider ISPs as this subclass is the inter-cross class including some LSPs and HSPs), and the results are listed in table 3.

When the multiple linear regression analysis is performed for the de-beamed luminosity subsample of 353 blazars with available Doppler factor, for a continuous jet, we have

$$\log L_\gamma^{\text{inc}} = (0.34 \pm 0.03) \log L_R^{\text{inc}} + (0.40 \pm 0.04) \log L_O^{\text{inc}} + (0.17 \pm 0.03) \log L_X^{\text{inc}} + (3.69 \pm 0.77),$$

with  $r = 0.93$ ,  $p < 0.001$ ,  $T_R^{\text{inc}} = 12.67$ ,  $T_O^{\text{inc}} = 10.51$ , and  $T_X^{\text{inc}} = 5.36$ . This method is also performed for the subclasses, and the results are listed in table 4. For a spherical jet, we have

$$\log L_\gamma^{\text{ins}} = (0.33 \pm 0.03) \log L_R^{\text{ins}} + (0.42 \pm 0.04) \log L_O^{\text{ins}} + (0.18 \pm 0.03) \log L_X^{\text{ins}} + (3.44 \pm 0.61),$$

with  $r = 0.96$ ,  $p < 0.001$ ,  $T_R^{\text{ins}} = 11.86$ ,  $T_O^{\text{ins}} = 11.22$ , and  $T_X^{\text{ins}} = 5.55$ . This method is also performed for the subclasses, and the results are listed in table 5.

To provide a clearer comparison of the  $T$  values from multiple linear regression analysis, in figure 1, we present the  $T$  values from the observed luminosities, intrinsic luminosities (for both continuous and spherical jet models), and the observed luminosities of 3FGL Fermi blazars from Zhang et al. (2018).

**Table 3.** Multiple regression results for observed luminosity.\*

Class (1)	$a \pm \Delta a$ (2)	$b \pm \Delta b$ (3)	$c \pm \Delta c$ (4)	$d \pm \Delta d$ (5)	N (6)	r (7)	p (8)	$T_R$ (9)	$T_O$ (10)	$T_X$ (11)
ALL	$0.53 \pm 0.03$	$0.56 \pm 0.05$	$0.14 \pm 0.03$	$-8.79 \pm 1.10$	642	0.93	<0.001	20.28	11.24	4.99
FSRQ	$0.63 \pm 0.08$	$0.45 \pm 0.09$	$0.17 \pm 0.07$	$-9.74 \pm 2.54$	227	0.85	<0.001	7.91	4.81	2.62
BLL	$0.47 \pm 0.04$	$0.65 \pm 0.06$	$0.11 \pm 0.03$	$-8.69 \pm 1.22$	415	0.92	<0.001	12.85	10.81	3.49
HBL	$0.27 \pm 0.06$	$0.82 \pm 0.08$	$0.12 \pm 0.04$	$-8.94 \pm 1.42$	289	0.91	<0.001	4.32	10.77	3.19
LBL	$0.41 \pm 0.18$	$0.47 \pm 0.23$	$0.19 \pm 0.17$	$-1.64 \pm 4.04$	38	0.91	<0.001	2.31	1.98	1.15
LF	$0.69 \pm 0.09$	$0.41 \pm 0.10$	$0.20 \pm 0.07$	$-11.65 \pm 2.85$	185	0.85	<0.001	7.56	4.02	2.79
HSP	$0.27 \pm 0.06$	$0.82 \pm 0.07$	$0.12 \pm 0.04$	$-9.03 \pm 1.42$	291	0.91	<0.001	4.41	10.99	3.19
LSP	$0.63 \pm 0.08$	$0.39 \pm 0.09$	$0.19 \pm 0.07$	$-7.81 \pm 2.33$	223	0.91	<0.001	7.68	4.20	2.84

\*The multiple regression is in the form  $\log L_\gamma = a \log L_R + b \log L_O + c \log L_X + d$ . Columns: (1) classification; (2)–(5) regression constant, slope, and their corresponding uncertainties; (6) sample size; (7) correlation coefficient; (8) chance probability; (9)–(11)  $T$  values for the radio, optical, and X-ray bands.

**Table 4.** Multiple regression results for de-beamed luminosity of a continuous jet.\*

Class (1)	$a \pm \Delta a$ (2)	$b \pm \Delta b$ (3)	$c \pm \Delta c$ (4)	$d \pm \Delta d$ (5)	N (6)	r (7)	p (8)	$T_R^{\text{inc}}$ (9)	$T_O^{\text{inc}}$ (10)	$T_X^{\text{inc}}$ (11)
ALL	$0.34 \pm 0.03$	$0.40 \pm 0.04$	$0.17 \pm 0.03$	$3.69 \pm 0.77$	353	0.93	<0.001	12.67	10.51	5.36
FSRQ	$0.56 \pm 0.07$	$0.33 \pm 0.07$	$0.07 \pm 0.06$	$2.31 \pm 1.04$	188	0.95	<0.001	8.04	4.87	1.27
BLL	$0.28 \pm 0.05$	$0.40 \pm 0.07$	$0.22 \pm 0.04$	$4.45 \pm 1.46$	165	0.92	<0.001	5.84	5.40	4.93
HBL	$0.30 \pm 0.10$	$0.51 \pm 0.11$	$0.14 \pm 0.06$	$2.41 \pm 1.89$	97	0.91	<0.001	2.99	4.45	2.41
LBL	$0.25 \pm 0.27$	$0.18 \pm 0.33$	$0.40 \pm 0.31$	$6.80 \pm 4.62$	25	0.91	<0.001	0.99	0.54	1.28
LF	$0.58 \pm 0.08$	$0.32 \pm 0.08$	$0.06 \pm 0.06$	$2.56 \pm 1.25$	156	0.94	<0.001	7.24	4.31	0.94
HSP	$0.30 \pm 0.10$	$0.51 \pm 0.12$	$0.14 \pm 0.06$	$2.41 \pm 1.89$	97	0.91	<0.001	2.99	4.45	2.41
LSP	$0.55 \pm 0.08$	$0.32 \pm 0.07$	$0.08 \pm 0.05$	$2.69 \pm 1.14$	181	0.94	<0.001	7.42	4.84	1.43

\*The multiple regression is in the form  $\log L_\gamma^{\text{inc}} = a \log L_R^{\text{inc}} + b \log L_O^{\text{inc}} + c \log L_X^{\text{inc}} + d$ . The continuous jet model corrects the observed luminosity in  $L_\nu^{\text{inc}} = L_\nu^{\text{ob}} / \delta^{3+\alpha_\nu}$ . Columns: (1) classification; (2)–(5) regression constant, slope, and their corresponding uncertainties; (6) sample size; (7) correlation coefficient; (8) chance probability; (9)–(11)  $T$  values for the radio, optical, and X-ray bands, respectively.

**Table 5.** Multiple regression results for de-beamed luminosity of a spherical jet.\*

Class (1)	$a \pm \Delta a$ (2)	$b \pm \Delta b$ (3)	$c \pm \Delta c$ (4)	$d \pm \Delta d$ (5)	N (6)	r (7)	p (8)	$T_R^{\text{ins}}$ (9)	$T_O^{\text{ins}}$ (10)	$T_X^{\text{ins}}$ (11)
ALL	$0.33 \pm 0.03$	$0.42 \pm 0.04$	$0.18 \pm 0.03$	$3.44 \pm 0.61$	353	0.96	<0.001	11.86	11.22	5.55
FSRQ	$0.54 \pm 0.07$	$0.35 \pm 0.07$	$0.07 \pm 0.06$	$2.20 \pm 0.83$	188	0.97	<0.001	7.68	4.97	1.32
BLL	$0.25 \pm 0.05$	$0.42 \pm 0.07$	$0.23 \pm 0.04$	$4.77 \pm 1.15$	165	0.95	<0.001	5.02	5.85	5.24
HBL	$0.26 \pm 0.10$	$0.50 \pm 0.11$	$0.15 \pm 0.06$	$3.48 \pm 1.53$	97	0.94	<0.001	2.66	4.49	2.67
LBL	$0.24 \pm 0.24$	$0.21 \pm 0.32$	$0.42 \pm 0.30$	$6.18 \pm 3.69$	25	0.94	<0.001	0.99	0.64	1.37
LF	$0.56 \pm 0.08$	$0.33 \pm 0.08$	$0.06 \pm 0.06$	$2.40 \pm 0.98$	156	0.96	<0.001	6.90	4.40	0.99
HSP	$0.26 \pm 0.10$	$0.50 \pm 0.11$	$0.15 \pm 0.06$	$3.48 \pm 1.54$	97	0.94	<0.001	2.66	4.49	2.67
LSP	$0.53 \pm 0.08$	$0.34 \pm 0.07$	$0.08 \pm 0.06$	$2.51 \pm 0.90$	181	0.96	<0.001	7.06	4.97	1.53

\*The multiple regression is in the form  $\log L_\gamma^{\text{ins}} = a \log L_R^{\text{ins}} + b \log L_O^{\text{ins}} + c \log L_X^{\text{ins}} + d$ . The spherical jet model corrects the observed luminosity in  $L_\nu^{\text{ins}} = L_\nu^{\text{ob}} / \delta^{4+\alpha_\nu}$ . Columns: (1) classification; (2)–(5) regression constant, slope, and their corresponding uncertainties; (6) sample size; (7) correlation coefficient; (8) chance probability; (9)–(11)  $T$  values for the radio, optical, and X-ray bands, respectively.

### 3 Discussion

#### 3.1 Observed luminosity correlations

Correlations between the  $\gamma$ -rays and the lower-energy bands have been investigated by many authors (Dondi & Ghisellini 1995; Giroletti et al. 2010; Fan et al. 2016; Lin et al. 2017; Yang et al. 2017; Zhang et al. 2018). Xie et al. (1998) found that there is a weak correlation between the  $\gamma$ -ray and the X-ray bands and no correlation between the  $\gamma$ -ray and the optical or radio bands for 26 blazars. Cheng et al. (2000) found that positive correlations exist between radio and  $\gamma$ -ray bands and no correlations exist between the optical, X-ray, and  $\gamma$ -ray band for 61 blazars. Fan et al. (2016) found that there are correlations between the  $\gamma$ -ray emissions and the radio, optical, and the X-ray emissions for 39 blazars. Yang et al. (2017) found a positive correlation between the  $\gamma$ -ray and the synchrotron peak luminosity for BLLs. Zhang et al. (2018) found correlations between the  $\gamma$ -ray emissions and the radio, opti-

cal, and the X-ray emissions for a sample of 442 blazars, with the radio emissions being the most important.

Following the above investigating method, we adopted the ordinary least-squares (OLS) multiple linear regression method used by Fan (1996), revisiting a sample of 642 sources with available luminosities and redshift. For the whole sample, the parameter  $T$  for the radio, optical, and X-ray emissions are 20.28, 11.24, and 4.99, with a correlation coefficient of  $r = 0.93$ . The  $T$  values show  $T_R \sim 4.07 T_X$  and  $T_O \sim 2.25 T_X$ , revealing that all the lower-energy bands are important for the  $\gamma$ -rays, and that the radio emission is the most important, followed by the optical emission and the X-ray emissions.

When we consider the subclasses, as shown in figure 1, the  $T$  values are all greater than unity, indicating that all the lower-energy bands are important for the  $\gamma$ -ray emissions. For FSRQs, BLLs, LBLs, LFs, and LSPs, the radio emissions hold the primary significance, followed by the optical emissions, which are more important than the X-ray emissions. For HBLs

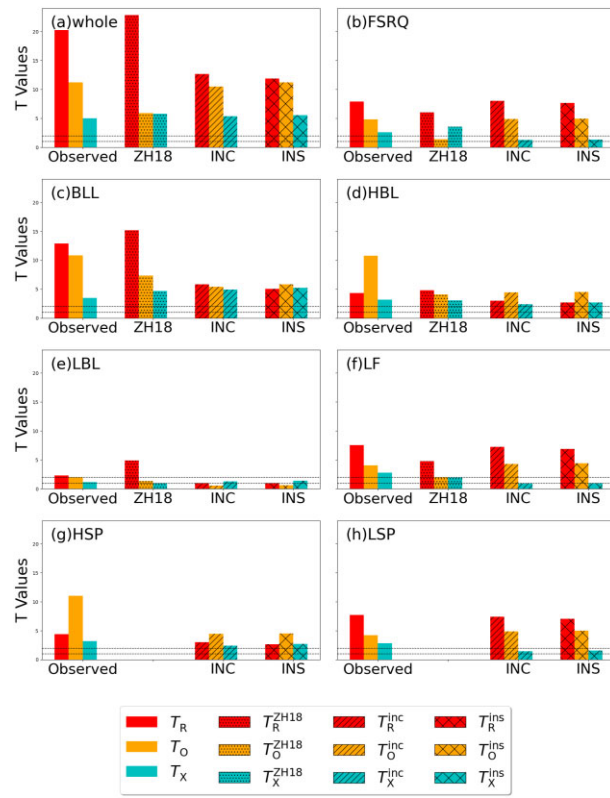


**Fig. 1.**  $T$  values from multiple regression analysis for the whole sample and different subclasses: (a) whole sample, (b) FSRQ, (c) BLL, (d) HBL, (e) LBL, (f) LF, (g) HSP, and (h) LSP. The red, orange, and cyan bars represent the  $T$  values for the radio, optical, and X-ray bands, respectively. The solid bars represent the  $T$  values calculated from the observed luminosity; the dotted bars represent the  $T$  values from Zhang et al. (2018), based on observed luminosities of 3FGL blazars; while the slashed and crosshatched bars correspond to the  $T$  values from intrinsic luminosities for a continuous jet and a spherical jet, respectively. For the (g) HSP and (h) LSP panels, the analysis of these two subclasses was not included in the study by Zhang et al. (2018). The dashed lines indicate thresholds for statistical significance:  $T = 1.0$  (moderate importance) and  $T = 2.0$  (substantial importance).

and HSPs, the optical emissions hold the most importance, followed by the radio emissions.

The present results are consistent with Fan (1996), who show that the radio band is the most significant for  $\gamma$ -ray emissions for the whole sample of 28 blazars. These results are also consistent with Zhang et al. (2018) except for FSRQs and HBLs. The data used in the work by Zhang et al. (2018) are from the 3FGL catalog<sup>2</sup> (extracted from Fan et al. 2016), which is based on the observations of the first four years. In contrast, the present work used the 4FGL-DR3 catalog<sup>3</sup> (extracted from Yang et al. 2022a), which is based on 12 years of observations. Given that FSRQs exhibit stronger variability than BLLs in the optical (Zhang et al. 2015; Yang et al. 2022c) and the  $\gamma$ -ray (Rajput et al. 2020) bands, the relatively longer observation data in the present work reduce the interference caused by variability and provide greater statistical reliability for the FSRQs. For HBLs, the optical band is the most significant for  $\gamma$ -ray emissions in present work, while the radio band is the most important. The SED of the blazars exhibits a double-peak structure. For HBLs, compared with the

radio band frequency [ $\log(\nu_R/\text{Hz}) = 9.19$ ], the optical band frequency [ $\log(\nu_O/\text{Hz}) = 14.39$ ] is closer to the average synchrotron peak frequency [ $\log(\nu_p/\text{Hz}) = 16.07 \pm 0.67$ ]. This implies that the seed photons for  $\gamma$ -rays for HBLs through the SSC model primarily originate from the optical band, meaning that the optical band holds more importance for  $\gamma$ -ray emissions. Our sample size for HBLs (289 HBLs) is more than three times larger than that in Zhang et al. (2018)—that is, 88 HBLs—making the present sample more comprehensive. Our result is consistent with Fan et al. (2016) and Yang et al. (2022a), who both found that the correlation between the optical and  $\gamma$ -ray bands is closer than that between the radio and  $\gamma$ -ray bands for HBLs.

Given that the 291 HSPs are predominantly composed of 289 HBLs, the optical band also plays the most important role in the  $\gamma$ -ray emissions, followed by the radio band.

To make a further study of the  $\gamma$ -ray emission dependence on the radio, optical, and X-ray bands, the mutual correlations in the form  $\log L_\gamma = e + f \log L_j$  are also investigated, in which the parameter  $j$  in  $L_j$  stands for the radio, optical, or X-ray band;  $e$  is a constant and  $f$  is a regression coefficient. We also calculated the correlation coefficient  $r$  and the corresponding chance probability  $p$ . The parameters for the mutual correlations for the whole sample and subclasses are listed in table 6. The plot of the correlation between the  $\gamma$ -ray band and the lower-energy bands for the whole sample and subclasses are shown in figure 2.

It is known that the dependence of the luminosity on redshift will affect the luminosity–luminosity correlation, so the redshift effect should be removed in a real luminosity–luminosity correlation. We approached the partial correlation by Padovani (1992) to remove the redshift effect. For variables  $i$ ,  $j$ , and  $z$ , when  $i$  and  $j$  are both correlated with  $z$ , then the effects of variable  $z$  should be removed. We calculated the partial correlation coefficients in the form

$$r_{ij,z} = \frac{r_{ij} - r_{iz}r_{jz}}{\sqrt{1 - r_{iz}^2}\sqrt{1 - r_{jz}^2}}, \quad (1)$$

where  $r_{ij}$ ,  $r_{iz}$ , and  $r_{jz}$  stand for the mutual correlation coefficients between  $i$  and  $j$ ,  $i$  and  $z$ , and  $j$  and  $z$ , respectively. The correlation coefficients after removing the redshift are listed in columns 6 and 7 in table 6. When the redshift effect is removed, the correlation coefficients reduce for the whole sample and all the subclasses. The correlations exist even after removing the redshift effect for the subclasses except in  $\log L_\gamma - \log L_X$  for the whole sample with  $p_{\gamma X,z} = 0.997$  and for BLLs with  $p_{\gamma X,z} = 0.353$ .

In general, for the whole sample and all the subclasses, the lower-energy bands are all correlated with the  $\gamma$ -ray emissions. Especially for the radio band, a positive correlation ( $r > 0.37$ ,  $p < 0.026$ ) still exists after the redshift effect is removed. From the lepton model, the high-energy  $\gamma$ -rays originate from the low-energy radio photons through the SSC processes where the photons get energies in scattering (Maraschi et al. 1992; Sikora et al. 1994). Thus, if there are parts of  $\gamma$ -ray emission generated by SSC processes, correlations between the radio and  $\gamma$ -ray emissions can be expected. Dondi and Ghisellini (1995) found that there is a good correlation between the  $\gamma$ -ray and the radio bands in  $\gamma$ -ray-loud blazars. Fan et al. (1998) and Zhang et al. (2018) also found that radio emissions are the most significant for  $\gamma$ -ray emissions. Meanwhile, the optical band is of following importance,

<sup>2</sup> [https://fermi.gsfc.nasa.gov/ssc/data/access/lat/4yr\\_catalog/](https://fermi.gsfc.nasa.gov/ssc/data/access/lat/4yr_catalog/).

<sup>3</sup> [https://fermi.gsfc.nasa.gov/ssc/data/access/lat/12yr\\_catalog/](https://fermi.gsfc.nasa.gov/ssc/data/access/lat/12yr_catalog/).

**Table 6.** Observed correlation analysis results:  $L_\gamma - (L_R/L_O/L_X)$ .\*

$\log L_\gamma - \log L_j$ (1)	Class (2)	Num (3)	$r_{\gamma-j}$ (4)	$p_{\gamma j}$ (5)	$r_{\gamma j, z}$ (6)	$p_{\gamma j, z}$ (7)
$\log L_\gamma - \log L_R$	ALL	642	0.90	<0.001	0.64	<0.001
	FSRQ	227	0.82	<0.001	0.42	<0.001
	BLL	415	0.86	<0.001	0.65	<0.001
	LBL	38	0.87	<0.001	0.37	0.026
	HBL	289	0.84	<0.001	0.56	<0.001
	LF	185	0.82	<0.001	0.43	<0.001
	HSP	291	0.84	<0.001	0.55	<0.001
	LSP	223	0.83	<0.001	0.40	<0.001
	ALL	642	0.89	<0.001	0.52	<0.001
	FSRQ	227	0.78	<0.001	0.31	<0.001
$\log L_\gamma - \log L_O$	BLL	415	0.89	<0.001	0.63	<0.001
	LBL	38	0.88	<0.001	0.45	0.005
	HBL	289	0.90	<0.001	0.68	<0.001
	LF	185	0.77	<0.001	0.34	<0.001
	HSP	291	0.90	<0.001	0.68	<0.001
	LSP	223	0.79	<0.001	0.33	<0.001
	ALL	642	0.66	<0.001	$-1.44 \times 10^{-4}$	0.997
	FSRQ	227	0.67	<0.001	0.19	0.004
	BLL	415	0.65	<0.001	0.05	0.353
	LBL	38	0.84	<0.001	0.34	0.003
$\log L_\gamma - \log L_X$	HBL	289	0.75	<0.001	0.27	<0.001
	LF	185	0.67	<0.001	0.21	0.003
	HSP	291	0.75	<0.001	0.27	<0.001
	LSP	223	0.71	<0.001	0.21	0.002

\*Columns: (1)  $\log L_\gamma - \log L_j$ , where  $j$  stands for the radio, optical, and X-ray; (2) classification; (3) sample size; (4) and (5) correlation coefficients and chance probability, where  $j$  stands for the radio, optical, and X-ray, respectively; (6) and (7) correlation coefficient and chance probability, where  $j$  stands for the radio, optical, and X-ray, after removing the redshift effect.

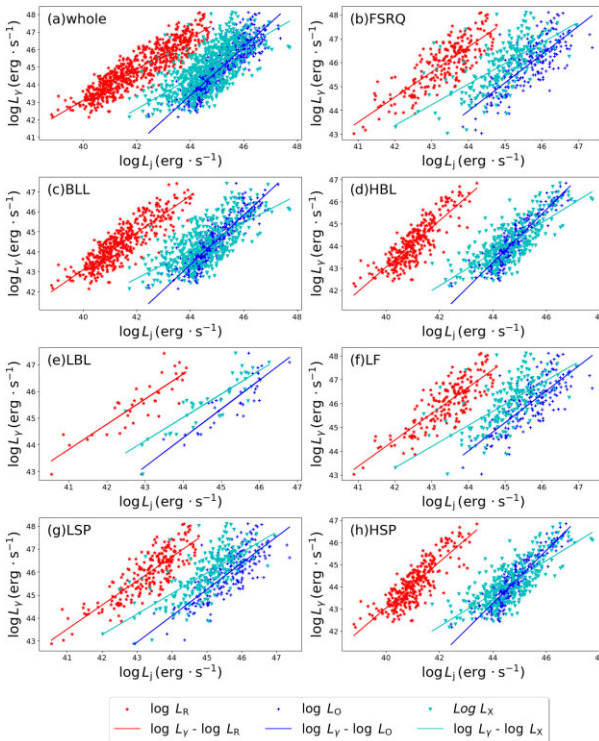


**Fig. 2.** Plot of the observed luminosity correlation between the  $\gamma$ -ray and lower-energy bands. This figure shows the observed luminosity correlations for the whole sample and different subclasses: (a) whole sample, (b) FSRQ, (c) BLL, (d) HBL, (e) LBL, (f) LF, (g) LSP, and (h) HSP. The red stars, blue daggers, and cyan inverted triangles represent  $\log L_\gamma - \log L_R$ ,  $\log L_\gamma - \log L_O$ , and  $\log L_\gamma - \log L_X$ , respectively. The corresponding regression lines are shown in red, blue, and cyan, respectively.

where the correlation coefficients after removing the redshift effect are all greater than 0.31, with  $p$  values all smaller than 0.005. For the  $\gamma$ -rays and the X-rays, there are strong correlations for the whole sample and the subclasses, but there is no correlation for the whole sample with  $p_{\gamma X,z} = 0.997$ , or BLLs with  $p_{\gamma X,z} = 0.353$  after removing the redshift effect.

For FSRQs, there are only two HSPs, and they are dominated by LSPs. As shown in table 6, positive correlations are found between the lower-energy bands (radio, optical, and X-ray) and the  $\gamma$ -ray band ( $r_{\gamma R,z} = 0.42$  with  $p_{\gamma R,z} < 0.001$ ,  $r_{\gamma O,z} = 0.31$  with  $p_{\gamma O,z} < 0.001$ , and  $r_{\gamma X,z} = 0.19$  with  $p_{\gamma X,z} = 0.004$ ). For HBLs, positive correlations are observed between the lower-energy bands and the  $\gamma$ -ray band ( $r_{\gamma R,z} = 0.56$  with  $p_{\gamma R,z} < 0.001$ ,  $r_{\gamma O,z} = 0.68$  with  $p_{\gamma O,z} < 0.001$ , and  $r_{\gamma X,z} = 0.27$  with  $p_{\gamma X,z} < 0.001$ ). These results are consistent with the expectation of the one-zone lepton model, in which the  $\gamma$ -ray emissions are primarily produced via SSC or SSC + EC processes. For LBLs, there are only 38 sources but about one-third of them are changing-look blazars, lacking the statistical significance.

The LSPs, ISPs, and HSPs occupy different regions in the  $\log L_\gamma - \log L_X - \log z$  parameter space (shown in the top panel in figure 5), which can be attributed to the blazar sequence and selection effects. The blazar sequence suggests an inverse correlation between luminosity and synchrotron peak frequency (Fossati et al. 1998; Fan et al. 2017; Yang et al. 2022b). Additionally, flux-limited selection biases favor the detection of LSPs at higher redshifts, while HSPs are predominantly observed at lower redshifts (see table 1;  $\bar{z} = 0.39 \pm 0.40$  for HSPs,  $\bar{z} = 0.56 \pm 0.52$  for ISPs, and  $\bar{z} = 0.95 \pm 0.54$  for LSPs). Although each subclass exhibits a correlation between

**Table 7.** De-beamed correlation analysis results.\*

$\log L_{\gamma}^{\text{in}} - \log L_k^{\text{in}}$ (1)	Class (2)	Num (3)	$r_{\gamma-k}^{\text{inc}}$ (4)	$p_{\gamma-k}^{\text{inc}}$ (5)	$r_{\gamma k, zd}^{\text{inc}}$ (6)	$p_{\gamma k, zd}^{\text{inc}}$ (7)	$r_{\gamma-k}^{\text{ins}}$ (8)	$p_{\gamma-k}^{\text{ins}}$ (9)	$r_{\gamma k, zd}^{\text{ins}}$ (10)	$p_{\gamma k, zd}^{\text{ins}}$ (11)
$\log L_{\gamma}^{\text{in}} - \log L_R^{\text{in}}$	ALL	353	0.83	<0.001	0.41	<0.001	0.88	<0.001	0.41	<0.001
	FSRQ	188	0.93	<0.001	0.48	<0.001	0.96	<0.001	0.48	<0.001
	BLL	165	0.71	<0.001	0.33	<0.001	0.80	<0.001	0.33	<0.001
	LBL	25	0.87	<0.001	0.40	0.063	0.91	<0.001	0.40	0.063
	HBL	97	0.86	<0.001	0.55	<0.001	0.89	<0.001	0.55	<0.001
	LF	156	0.93	<0.001	0.48	<0.001	0.96	<0.001	0.48	<0.001
	HSP	97	0.86	<0.001	0.55	<0.001	0.89	<0.001	0.55	<0.001
	LSP	181	0.93	<0.001	0.47	<0.001	0.95	<0.001	0.47	<0.001
$\log L_{\gamma}^{\text{in}} - \log L_O^{\text{in}}$	ALL	353	0.90	<0.001	0.53	<0.001	0.93	<0.001	0.53	<0.001
	FSRQ	188	0.93	<0.001	0.45	<0.001	0.95	<0.001	0.45	<0.001
	BLL	165	0.89	<0.001	0.63	<0.001	0.93	<0.001	0.63	<0.001
	LBL	25	0.89	<0.001	0.60	0.002	0.93	<0.001	0.60	0.002
	HBL	97	0.90	<0.001	0.67	<0.001	0.93	<0.001	0.67	<0.001
	LF	156	0.92	<0.001	0.46	<0.001	0.95	<0.001	0.46	<0.001
	HSP	97	0.90	<0.001	0.67	<0.001	0.93	<0.001	0.67	<0.001
	LSP	181	0.92	<0.001	0.48	<0.001	0.95	<0.001	0.48	<0.001
$\log L_{\gamma}^{\text{in}} - \log L_X^{\text{in}}$	ALL	353	0.86	<0.001	0.24	<0.001	0.91	<0.001	0.24	<0.001
	FSRQ	188	0.89	<0.001	0.21	0.003	0.93	<0.001	0.21	0.003
	BLL	165	0.83	<0.001	0.35	<0.001	0.89	<0.001	0.35	<0.001
	LBL	25	0.90	<0.001	0.58	<0.001	0.94	<0.001	0.58	<0.001
	HBL	97	0.81	<0.001	0.36	<0.001	0.86	<0.001	0.36	<0.001
	LF	156	0.87	<0.001	0.20	0.011	0.92	<0.001	0.20	0.011
	HSP	97	0.81	<0.001	0.36	<0.001	0.86	<0.001	0.36	<0.001
	LSP	181	0.88	<0.001	0.20	0.006	0.92	<0.001	0.20	0.006

\*Columns: (1)  $\log L_{\gamma}^{\text{in}} - \log L_k^{\text{in}}$ , where  $k$  stands for the radio, optical, and X-ray bands, respectively; (2) classification; (3) sample size; (4) and (5) correlation coefficients and chance probability for the continuous jet, where  $k$  stands for the radio, optical, and X-ray bands, respectively; (6) and (7) correlation coefficient and chance probability, where  $k$  stands for the radio, optical, and X-ray bands, respectively, after removing the redshift and the effect of Doppler factor for the continuous jet; (8) and (9) correlation coefficients and chance probability for the spherical jet, where  $k$  stands for the radio, optical, and X-ray bands, respectively; (10) and (11) correlation coefficient and chance probability, where  $k$  stands for the radio, optical, and X-ray bands, respectively, after removing the redshift and the effect of Doppler factor for the spherical jet.

the X-ray and  $\gamma$ -ray luminosities, their slopes in the  $\log L_{\gamma} - \log L_X - \log z$  parameter space are different. When projected on to the  $\log L_{\gamma} - \log L_X$  plane and visualized using redshift-corrected residuals (shown in the upper panel of figure 5), the distinct positional separation persists, leading to an uneven sample distribution, which tends to dilute the overall correlation.

We see that there is a correlation for LBLs, and that there is also a correlation for HBLs between the X-ray and the  $\gamma$ -ray bands. However, there is no correlation for 415 BLLs with  $r_{\gamma X, z} = 0.05$  and  $p_{\gamma X, z} = 0.353$ . We suggest that the reason for this is similar to what is discussed above, namely that the combination of distinct subclasses occupying different regions dilutes the correlation. The 415 BLLs in our sample include 289 HBLs, 88 IBLs, and 38 LBLs, particularly aligning with the composition of the whole sample, which includes 291 HSPs, 128 ISPs, and 223 LSPs.

In our sample, the radio band is at  $1.4 \times 10^9$  Hz, the optical band is at  $2.43 \times 10^{14}$  Hz, the X-ray band is at  $2.4 \times 10^{17}$  Hz (1 keV), and the  $\gamma$ -ray band is at  $2.4 \times 10^{23}$  Hz (1 GeV). From Prandini and Ghisellini (2022), the more powerful blazars primarily emit X-rays via the IC process, whereas less powerful blazars predominantly produce X-rays through synchrotron radiation. In the X-ray band, both the synchrotron and IC processes can contribute to the emission (Ghisellini & Tavecchio 2008), and hence for all subclasses, the X-ray band holds the least importance.

### 3.2 Intrinsic luminosity correlations

When removed the beaming effect, as shown in figure 1, for the whole sample, FSRQs, LFs, and LSPs, the radio bands are

the most important for the  $\gamma$ -ray emissions, followed by the optical bands for both the continuous jet and spherical jet models. For HBLs and HSPs, the optical bands have primary significance for the  $\gamma$ -ray emissions for both the continuous jet and spherical jet model. For the whole sample, FSRQs, BLLs, HBLs, HSPs, and LSPs, all the lower-energy bands are important for the  $\gamma$ -ray emissions for both the continuous jet and spherical jet model. The intrinsic multiple correlations are consistent with the observed results, except for BLLs, LBLs, and LFs.

For BLLs, the de-beamed  $T$  values for the continuous jet indicate that the radio band holds the most importance for the  $\gamma$ -ray emissions, followed by the optical band, in agreement with the observed luminosities. However, for the spherical jet, the de-beamed  $T$  values show that the optical band holds the most importance for  $\gamma$ -ray emissions. The  $T$ -value ratio of radio or optical to the X-ray band are very close to unity (within 20%). Considering the error derived from the two different models and observation errors in luminosity, we think that all the radio, optical, and X-ray bands are approximately equally important for the  $\gamma$ -ray emissions. Some BLLs exhibit emission lines while others do not, leading to a selection effect in our intrinsic sample (415 BLLs are included in the observed luminosity analysis, but only 165 are available for the intrinsic luminosity analysis), which partly affects the intrinsic correlation results.

For LBLs, the de-beamed  $T$  values show that the X-ray band holds most importance for  $\gamma$ -ray emissions, but  $T_R^{\text{inc}}$ ,  $T_O^{\text{inc}}$ ,  $T_R^{\text{ins}}$ , and  $T_O^{\text{ins}}$  are all less than 1.0, indicating that radio and optical bands are not important for  $\gamma$ -ray emission. This is inconsistent with the observed luminosities. There are only 25

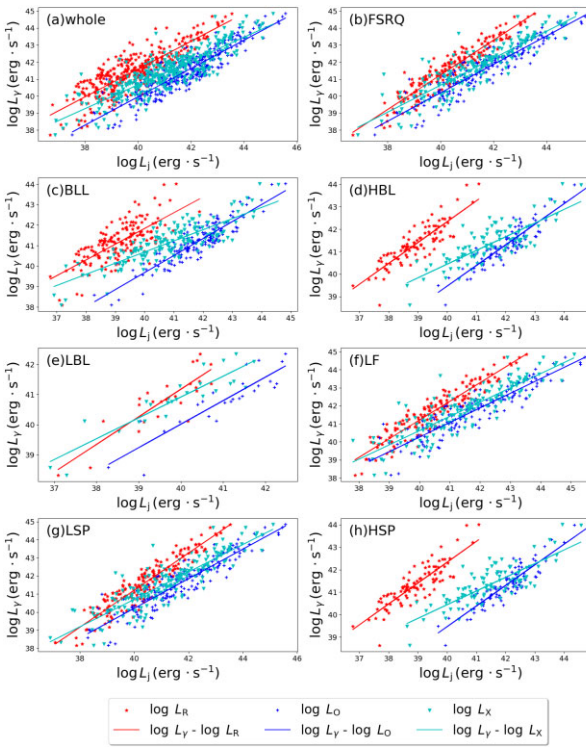


**Fig. 3.** Plot of the intrinsic luminosity correlation for a continuous jet. This figure illustrates the intrinsic luminosity correlations for a continuous jet between the  $\gamma$ -ray and lower-energy bands for the whole sample and different subclasses: (a) whole sample, (b) FSRQ, (c) BLL, (d) HBL, (e) LBL, (f) LF, (g) LSP, and (h) HSP. The red stars, blue daggers, and cyan inverted triangles represent  $\log L_\gamma^{\text{inc}} - \log L_R^{\text{inc}}$ ,  $\log L_\gamma^{\text{inc}} - \log L_O^{\text{inc}}$ , and  $\log L_\gamma^{\text{inc}} - \log L_X^{\text{inc}}$ , respectively. The corresponding regression lines are shown in red, blue, and cyan, respectively.

sources in this sample, and more than half are changing-look blazars (BLL to FSRQ), affecting the mutual correlations.

For LFs, the radio and optical bands are both important for  $\gamma$ -ray emissions, but X-ray emissions are not so important for the  $\gamma$ -ray emissions.  $T_X^{\text{inc}} = 0.94$  and  $T_{\text{X}}^{\text{ins}} = 0.99$  are close to unity (within 6%). Considering the observational uncertainties in luminosities, a possible association between the X-ray and  $\gamma$ -ray bands cannot be ruled out.

To further investigate whether the de-beamed  $\gamma$ -ray emission is dependent on the radio, optical, and X-ray bands, the mutual correlations in the form  $\log L_\gamma^{\text{inc}} = m + n \log L_k^{\text{inc}}$  for a continuous jet (or  $\log L_\gamma^{\text{ins}} = m + n \log L_k^{\text{ins}}$  for a spherical jet) are also investigated. Here, the parameter  $k$  in  $L_k^{\text{inc}}$  (or  $L_k^{\text{ins}}$ ) stands for the radio, optical, or X-ray band,  $m$  is a constant, and  $n$  is the regression coefficient. The results are shown in table 7. Figures 3 and 4 illustrate the correlation between the  $\gamma$ -ray band and the lower-energy band for a continuous jet and a spherical jet for the whole sample and subclasses. After de-beaming the luminosity ( $L_\nu^{\text{in}} = L_\nu^{\text{ob}} / \delta^{3+\alpha_v}$  for a continuous jet or  $L_\nu^{\text{in}} = L_\nu^{\text{ob}} / \delta^{4+\alpha_v}$  for a spherical jet), the luminosities are correlated with the Doppler factor ( $\delta$ ). In a real intrinsic luminosity-luminosity correlation, both the redshift ( $z$ ) and the effect of Doppler factor ( $\delta$ ) should be removed. We applied the second-order partial correlation coefficient (Padovani 1992):

$$r_{ij,zd} = \frac{r_{ij,z} - r_{id,z} r_{jd,z}}{\sqrt{(1 - r_{id,z}^2)(1 - r_{jd,z}^2)}}. \quad (2)$$

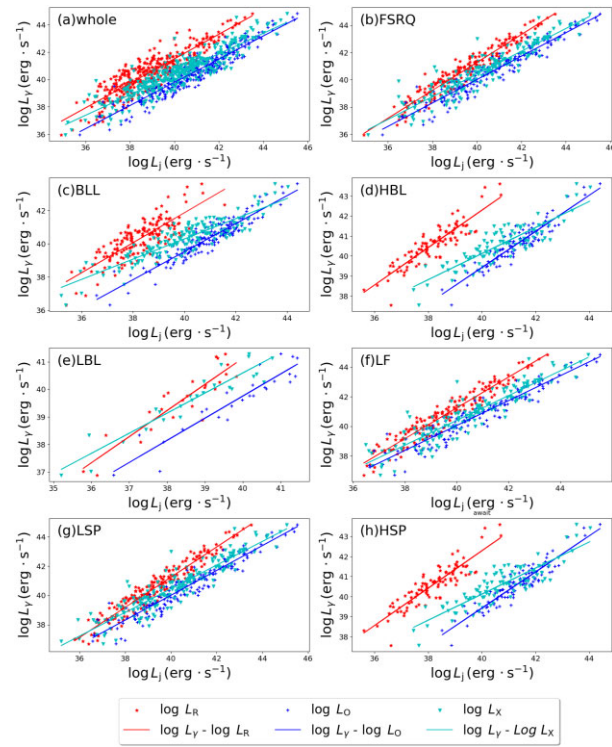


**Fig. 4.** Plot of the intrinsic luminosity correlation for a spherical jet. This figure displays the intrinsic luminosity correlations between the  $\gamma$ -ray and lower-energy bands for the whole sample and different subclasses: (a) whole sample, (b) FSRQ, (c) BLL, (d) HBL, (e) LBL, (f) LF, (g) LSP, and (h) HSP. The red stars, blue daggers, and cyan inverted triangles represent  $\log L_\gamma^{\text{ins}} - \log L_R^{\text{ins}}$ ,  $\log L_\gamma^{\text{ins}} - \log L_O^{\text{ins}}$ , and  $\log L_\gamma^{\text{ins}} - \log L_X^{\text{ins}}$ , respectively. The corresponding regression lines are shown in red, blue, and cyan, respectively.

Here,  $r_{ij,zd}$  represents the correlation between variables  $i$  and  $j$  after accounting for the effects of both variables  $z$  and  $d$ , and  $r_{ij,z}$  represent the first-order partial correlation coefficient that we used to remove the redshift effect, as shown in subsection 3.1. The second-order partial correlation coefficients are the same regardless of whether the redshift effect or the effect of Doppler factor is removed first. The second-order correlation coefficient and the corresponding significance are listed in columns 6 and 7 for a continuous jet, and in columns 10 and 11 for a spherical jet, in table 7.

In the blazar radiation model, the blob moves toward us at relativistic speeds, resulting in many extremely observational properties (Blandford & Königl 1979; Urry & Padovani 1995). When the blob's relativistic beaming effect is removed, the intrinsic correlation reveals the electron and photon radiation and acceleration mechanisms in the comoving frame.

Specifically, the intrinsic mutual correlations indicate that all lower-energy bands exhibit a strong correlation with the  $\gamma$ -ray band, with correlation coefficients  $r$  greater than 0.71 and  $p < 0.001$  for a continuous jet (or greater than 0.80 and  $p < 0.001$  for spherical jet). When removed the redshift and the effect of Doppler factor, the correlation coefficients reduce for the whole sample and all the subclasses especially in the X-ray band. Notably, the radio correlation for LBLs is relatively weak but also positive ( $r_{\gamma-R,zd}^{\text{inc}} = r_{\gamma-R,zd}^{\text{ins}} = 0.40$  and  $p_{\gamma-R,zd}^{\text{inc}} = p_{\gamma-R,zd}^{\text{ins}} = 0.063$ ). But this sample only include 25 sources, more than half of which are changing-look blazars, lacking the statistical significance. All the lower energy bands

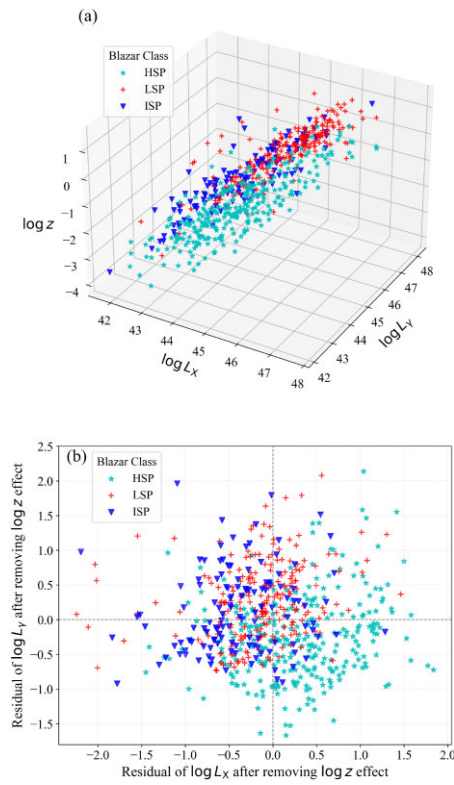


**Fig. 5.** (a) Three-dimensional distribution in the  $\log L_x$ – $\log L_y$ – $\log z$  parameter space. The cyan stars, blue inverted triangles, and red daggers represent the HSPs, ISPs, and LSPs, respectively. (b) Scatter plot of the residuals of  $\log L_y$  and  $\log L_x$  after removing the redshift. The cyan stars, blue inverted triangles and red daggers represent the HSPs, ISPs, and LSPs, respectively.

contribute significantly to  $\gamma$ -ray emissions, primarily due to the Doppler factor. The indices in the spherical jet intrinsic correction ( $4 + \alpha_v$ ) are greater than those in the continuous jet ( $3 + \alpha_v$ ), leading to higher intrinsic mutual correlation coefficients in the spherical jet compared to the continuous jet. It is confirmed that the correlation coefficients become the same after removing both the redshift and the effect of Doppler factor.

After removing both the redshift and Doppler factor effects, the real correlations are revealed, without the relativistic effects or the redshift. For FSRQs, which are dominated by LSPs, as shown in table 7, positive correlations are found between the lower-energy bands and the  $\gamma$ -ray band ( $r_{\gamma R,zd}^{\text{inc}} = r_{\gamma R,zd}^{\text{ins}} = 0.48$  with  $p_{\gamma R,zd}^{\text{inc}} = p_{\gamma R,zd}^{\text{ins}} < 0.001$ ,  $r_{\gamma O,zd}^{\text{inc}} = r_{\gamma O,zd}^{\text{ins}} = 0.45$  with  $p_{\gamma O,zd}^{\text{inc}} = p_{\gamma O,zd}^{\text{ins}} < 0.001$ , and  $r_{\gamma X,zd}^{\text{inc}} = r_{\gamma X,zd}^{\text{ins}} = 0.21$  with  $p_{\gamma X,zd}^{\text{inc}} = p_{\gamma X,zd}^{\text{ins}} = 0.003$ ). For HBLs, positive correlations are also observed between the lower-energy bands and the  $\gamma$ -ray band ( $r_{\gamma R,zd}^{\text{inc}} = r_{\gamma R,zd}^{\text{ins}} = 0.55$  with  $p_{\gamma R,zd}^{\text{inc}} = p_{\gamma R,zd}^{\text{ins}} < 0.001$ ,  $r_{\gamma O,zd}^{\text{inc}} = r_{\gamma O,zd}^{\text{ins}} = 0.67$  with  $p_{\gamma O,zd}^{\text{inc}} = p_{\gamma O,zd}^{\text{ins}} < 0.001$ , and  $r_{\gamma X,zd}^{\text{inc}} = r_{\gamma X,zd}^{\text{ins}} = 0.36$  with  $p_{\gamma X,zd}^{\text{inc}} = p_{\gamma X,zd}^{\text{ins}} < 0.001$ ). These results are consistent with the observed result, which is consistent with the theoretical expectations of the one-zone lepton model.

We find that there is a very strong correlation for LBLs between the X-ray and  $\gamma$ -ray emissions ( $r_{\gamma-X,zd}^{\text{inc}} = r_{\gamma-X,zd}^{\text{ins}} = 0.58$  and  $p_{\gamma-X,zd}^{\text{inc}} = p_{\gamma-X,zd}^{\text{ins}} < 0.001$ ), but there are weak cor-

relations for LSPs. We think the reason for this is that 25 LBLs is a small sample and more than half of those are changing-look blazars, which do not have statistical representation.

## 4 Conclusions

In this work, we extracted a sample of 642 blazars with known redshift and radio, optical, X-ray, and  $\gamma$ -ray luminosity, and studied the observed correlation between the  $\gamma$ -ray and lower-energy bands. Additionally, of 353 blazars with available Doppler factors, we also studied the intrinsic correlations between the  $\gamma$ -ray and lower-energy bands. Compared with previous studies, our work mainly focuses on the connection between the high-energy  $\gamma$ -ray and lower-energy (radio, optical, and X-ray) emissions, for both observed and intrinsic luminosities. Notably, the multiple intrinsic correlations are largely consistent with the observed ones (except for BLLs and LBLs), supporting the expectations of the leptonic emission model. Furthermore, we encourage readers to further discuss AGN unification schemes using the intrinsic correlation, which removed both the redshift and Doppler boosting effect. The main conclusions of this work are as follows.

1. The  $\gamma$ -ray emissions are correlated with all the lower-energy radio, optical and X-ray emissions. The redshift and the Doppler factor affect the mutual luminosity correlation, and should be excluded when a mutual luminosity correlation is investigated.
2. For the observed luminosity correlations, the radio emissions are the most important for the  $\gamma$ -ray emissions for the whole sample, and FSRQ, BLL, LBL, LF, and LSP subclasses, whereas the optical emissions are the most important for HBL and HSP subclasses. The X-ray emissions are the weakest for the  $\gamma$ -ray emissions for the whole sample and all the subclasses.
3. For the intrinsic luminosity correlations, the radio emissions are the most important for the  $\gamma$ -ray emissions for the whole sample, and FSRQ, LF, and LSP subclasses, while the optical emissions are the most important for the HBL and HSP subclasses. The X-ray emissions are the weakest for the  $\gamma$ -ray emissions for the whole sample, and the FSRQ, HBL, LF, HSP, and LSP subclasses.
4. When removing the beaming effect, the  $\gamma$ -ray emissions are also correlated with all the lower-energy radio, optical and X-ray emissions.
5. The radiation mechanisms for the blazars in our sample are consistent with the expectations of the one-zone lepton model, including SSC and EC processes.

## Funding

The work is partially supported by the National Natural Science Foundation of China (NSFC 12433004, U2031201), and the Eighteenth Regular Meeting Exchange Project of the Scientific and Technological Cooperation Committee between the People's Republic of China and the Republic of Bulgaria (series No. 1802). We also acknowledge the science research grants from the China Manned Space Project with No. CMS-CSST-2025-A07, and the support from the Astrophysics Key Subjects of Guangdong Province and Guangzhou City. The Natural Science Foundation of Guangdong Province (2024A1515013169) also supports this work.

## References

- Abdo, A. A., et al. 2010, ApJS, 188, 405  
 Ackermann, M., et al. 2015, ApJ, 810, 14  
 Aharonian, F. A. 2000, New Astron., 5, 377  
 Ajello, M., et al. 2022, ApJS, 263, 24  
 Angel, J. R. P., & Stockman, H. S. 1980, ARA&A, 18, 321  
 Antonucci, R. R. J., & Ulvestad, J. S. 1985, ApJ, 294, 158  
 Bachev, R., et al. 2023, MNRAS, 522, 3018  
 Beall, J. H., & Bednarek, W. 1999, ApJ, 510, 188  
 Blandford, R. D., & Königl, A. 1979, ApJ, 232, 34  
 Bloom, S. D., & Marscher, A. P. 1996, ApJ, 461, 657  
 Chen, G., Zheng, Z., Zeng, X., Zhang, L., Xiao, H., Liu, X., Cui, L., & Fan, J. 2024, ApJS, 271, 20  
 Cheng, K. S., Zhang, X., & Zhang, L. 2000, ApJ, 537, 80  
 Cohen, J. 1988, Statistical Power Analysis for the Behavioral Sciences, 2nd ed. (Hillsdale, NJ: Lawrence Erlbaum Associates)  
 Dermer, C. D., & Schlickeiser, R. 1993, ApJ, 416, 458  
 Dondi, L., & Ghisellini, G. 1995, MNRAS, 273, 583  
 Fallah Ramazani, V., Lindfors, E., & Nilsson, K. 2017, A&A, 608, A68  
 Fan, J. H. 1996, Ap&SS, 246, 119  
 Fan, J. H., et al. 2016, ApJS, 226, 20  
 Fan, J. H., et al. 2017, ApJ, 835, L38  
 Fan, J. H., Adam, G., Xie, G. Z., Cao, S. L., Lin, R. G., & Copin, Y. 1998, A&A, 338, 27  
 Fan, J. H., Yang, J. H., Zhang, Q. F., Li, Y., & Liu, Y. 2013, in Proc. IAU Symp. 290, Feeding Compact Objects: Accretion on All Scales, ed. C. M. Zhang et al. (Cambridge: Cambridge University Press), 207  
 Fossati, G., Maraschi, L., Celotti, A., Comastri, A., & Ghisellini, G. 1998, MNRAS, 299, 433  
 Ghisellini, G., & Tavecchio, F. 2008, MNRAS, 387, 1669  
 Ghisellini, G., Tavecchio, F., Foschini, L., & Ghirlanda, G. 2011, MNRAS, 414, 2674  
 Giroletti, M., Reimer, A., Fuhrmann, L., & Pavlidou, V. 2010, ASP Conf. Ser., 427, 283  
 Hovatta, T., et al. 2014, MNRAS, 439, 690  
 Konigl, A. 1981, ApJ, 243, 700  
 Lin, C., Fan, J-H., & Xiao, H-B. 2017, Res. Astron. Astrophys., 17, 066  
 Mannheim, K., & Biermann, P. L. 1992, A&A, 253, L21  
 Maraschi, L., Ghisellini, G., & Celotti, A. 1992, ApJ, 397, L5  
 Marscher, A. P., & Gear, W. K. 1985, ApJ, 298, 114  
 Padovani, P. 1992, A&A, 256, 399  
 Padovani, P., & Giommi, P. 1995, ApJ, 444, 567  
 Padovani, P., & Urry, C. M. 1991, BAAS, 23, 1344  
 Prandini, E., & Ghisellini, G. 2022, Galaxies, 10, 35  
 Rajput, B., Stalin, C. S., & Rakshit, S. 2020, A&A, 634, A80  
 Sikora, M., Begelman, M. C., & Rees, M. J. 1994, ApJ, 421, 153  
 Urry, C. M., & Padovani, P. 1995, PASP, 107, 803  
 Vermeulen, R. C., & Cohen, M. H. 1994, ApJ, 430, 467  
 Webb, W. B. 1992, PhD thesis, University of California, Los Angeles  
 Xiao, H., Ouyang, Z., Zhang, L., Fu, L., Zhang, S., Zeng, X., & Fan, J. 2022a, ApJ, 925, 40  
 Xiao, H. B., Zhu, J. T., Fan, J. H., Pei, Z. Y., Luo, Z. J., & Zhang, S. H. 2022b, MNRAS, 517, 4202  
 Xie, G. Z., Zhang, X., Bai, J. M., & Xie, Z. H. 1998, ApJ, 508, 180  
 Yang, J. H., Fan, J. H., Liu, Y., Zhang, Y. L., Yang, R. S., Tuo, M. X., Nie, J. J., & Yuan, Y. H. 2017, Ap&SS, 362, 219  
 Yang, J. H., et al. 2022a, ApJS, 262, 18  
 Yang, W. X., et al. 2022b, ApJ, 925, 120  
 Yang, W. X., Xiao, H. B., Wang, H. G., Yang, J. H., Pei, Z. Y., Wu, D. X., Yuan, Y. H., & Fan, J. H. 2022c, Res. Astron. Astrophys., 22, 085002  
 Zhang, B. K., Zhou, X. S., Zhao, X. Y., & Dai, B. Z. 2015, Res. Astron. Astrophys., 15, 1784  
 Zhang, L. X., & Fan, J. H. 2018, Ap&SS, 363, 142